aerospace

MDPI

Article

A Method for Detection and Three-Dimensional Localization of Spacecraft Electrostatic Discharge Events

Kai Tang [1], Haojie Zhang [1], Xiao Sun [2] and Xuqiang Lang [1,*]

[1] School of Mechanical and Electrical Engineering, Beijing Information Science and Technology University, Beijing 100192, China; tangkai@bistu.edu.cn (K.T.); zhhj241@163.com (H.Z.)
[2] The Astronaut Research and Training Center of China, Beijing 100094, China; daiguojun606@icloud.com
* Correspondence: langxuqiang@bistu.edu.cn

Abstract

Spacecraft electrostatic discharge (ESD) can generate transient electric-field disturbances, pulse currents, and electromagnetic coupling that threaten onboard electronics and mission reliability. Localizing discharge sources in confined spacecraft spaces remains difficult because conventional time-difference-of-arrival, radio-frequency, acoustic, and optical methods often require strict synchronization, large arrays, suitable propagation media, line-of-sight conditions, or explicit propagation models. This study develops a spacecraft-oriented, ground-validated electrostatic-induction sensor-array framework for three-dimensional localization of transient discharge events. Different from conventional received-signal-strength-based Apollonius localization, the proposed approach uses relative transient electrostatic-induction response features, including root-mean-square value, envelope energy, and integrated energy, and calibrates their feature ratios into distance-ratio constraints using a Power + offset mapping. These calibrated constraints are interpreted as Apollonius-sphere constraints, and the source coordinate is estimated by nonlinear residual minimization without relying on high-precision arrival-time picking. The method is evaluated on a controlled one-cubic-meter confined-space laboratory platform with known sensor geometry. Ten independent test positions show centimeter-level localization accuracy in the present calibration domain. The envelope-energy representation performs best, with a mean three-dimensional error of 7.01 cm, a median error of 6.94 cm, and a maximum error of 10.05 cm. These results demonstrate the feasibility of the sensing–calibration–inversion chain as a preliminary ground-based proof of concept. The reported accuracy should not be interpreted as direct on-orbit performance because the present experiment does not include vacuum, plasma, thermal gradients, spacecraft materials, metallic enclosures, or electronics integrated for spacecraft onboard operation; further environment-specific calibration and validation are required before practical spacecraft deployment.

Keywords: spacecraft electrostatic discharge; electrostatic induction sensor array; confined-space localization; feature ratio; distance ratio; Apollonius sphere; transient electric field; envelope energy

Check for updates

Academic Editor: Hyun-Ung Oh

Received: 27 May 2026
Revised: 1 July 2026
Accepted: 6 July 2026
Published: 10 July 2026

Copyright: © 2026 by the authors. Licensee MDPI, Basel, Switzerland. This article is an open access article distributed under the terms and conditions of the Creative Commons Attribution (CC BY) license.

1. Introduction

Spacecraft operate in plasma and radiation environments characterized by energetic charged particles, surface charging, internal dielectric charging, radiation exposure, and large temperature variations. Under these conditions, local potential differences

and strong electric fields may develop on external surfaces, dielectric components, cable harnesses, or internal structures, eventually triggering electrostatic discharge (ESD) events [1–3]. Mitigation handbooks and spacecraft-charging standards identify charging and discharge as persistent design concerns for spacecraft electrical and structural integration [4,5]. ESD events can generate fast current pulses, transient voltages, and broadband electromagnetic disturbances. Through grounding networks, structural coupling, cable harnesses, and sensitive electronic interfaces, these disturbances may cause data corruption, unintended triggering, temporary functional degradation, or system-level anomalies [6,7]. Recent spacecraft-charging reviews and internal-charging risk studies further show that charging-induced anomalies remain relevant for modern compact, high-power, and long-life spacecraft [8,9].

For spacecraft anomaly diagnosis, discharge detection alone is often insufficient. A detected transient confirms that an abnormal electromagnetic event has occurred, whereas localization further narrows the fault from a spacecraft-level anomaly to a specific region, structure, or component. Such spatial information can support root-cause tracing, grounding and shielding improvement, layout optimization, and ground reproduction tests. Classical spacecraft-charging design guidelines mainly emphasize mitigation and charging control, while recent studies have increasingly considered direct monitoring of discharge pulses and charging states [10–12]. Therefore, a localization-oriented sensing method is a useful extension of the existing mitigation-centered workflow. However, direct localization of spacecraft discharge events remains challenging because installation volume, mass, power, wiring resources, electromagnetic compatibility, and calibration opportunities are all constrained, and the discharge behavior is strongly dependent on mission-specific plasma, material, structural, and thermal conditions [13,14].

Existing discharge-localization methods provide useful references, but each has limitations when transferred to compact spacecraft compartments. Radio-frequency, ultra-high-frequency (UHF), and high-frequency current transformer (HFCT) methods are sensitive to fast discharge pulses and have been widely investigated in high-voltage equipment [15–17]; nevertheless, metallic boundaries, shielding structures, cable harnesses, and multipath coupling may complicate their use in confined spacecraft volumes. Time-difference-of-arrival (TDOA), received-signal-strength (RSS), received-signal-strength-difference (RSSD), and angle-based methods provide clear geometric constraints, but they generally require accurate timing, sufficiently separated arrays, stable propagation assumptions, or reliable path-loss models [18–21]. Acoustic methods require an appropriate propagation medium and stable structural coupling path, while optical or fiber-optic methods are limited when the discharge is occluded or not within the line of sight [22–24]. In addition, absolute-amplitude or absolute-energy indicators are vulnerable to source-strength fluctuation, channel-gain differences, and boundary coupling. These disadvantages motivate a compact, calibration-based approach that avoids explicit arrival-time picking and uses relative response information rather than absolute signal magnitude.

Electrostatic induction sensors are attractive for this purpose because they are structurally simple, fast-response, miniaturizable, and suitable for sensing transient electric-field disturbances [25–27]. Their use is also consistent with spacecraft-oriented electric-potential and electric-field measurement studies that emphasize compactness, wide dynamic range, and high-input-impedance sensing [14]. In response to the limitations discussed above, this study proposes a feature-ratio–distance-ratio localization framework based on a four-spherical-electrode electrostatic induction array. The contribution of this work is not the Apollonius geometry itself, which is a known ratio-based localization concept, but the construction of transient electrostatic-induction response features, the calibration of their multi-channel ratios into distance-ratio constraints, and the validation of

the complete sensing–calibration–inversion chain in a controlled confined-space platform. Compared with TDOA-based methods, the proposed framework reduces dependence on high-precision arrival-time picking; compared with conventional RSS-based Apollonius localization, it does not use a generic free-space path-loss law or absolute received strength, but uses experimentally calibrated electrostatic-induction feature ratios that can absorb fixed channel gain, array geometry, and boundary-coupling effects within a specified calibration domain.

The scope of this paper is a ground-based proof-of-concept validation rather than deployment-level qualification for operational spacecraft. The experiment is performed in ambient laboratory conditions using a repeatable needle–plate transient source and a one-cubic-meter confined-space platform. Therefore, the reported accuracy represents the performance of the proposed method under the present geometry, boundary, and calibration conditions, and it should not be generalized directly to in-orbit spacecraft without additional validation under vacuum, plasma, thermal, material, and structural conditions. The remainder of this paper is organized as follows: Section 2 gives an overview of the proposed localization framework. Section 3 presents the sensing model, feature-ratio construction, geometric inversion, and environmental applicability boundaries. Section 4 describes the laboratory validation platform and calibration design. Section 5 reports the calibration and localization results. Section 6 discusses the technical contribution, limitations, engineering implications, and future development. Section 7 concludes this paper.

2. Overview of the Proposed Localization Framework

The overall methodological chain is summarized in Figure 1. The framework begins with a localized transient discharge event that produces a rapidly varying electric-field disturbance in a confined volume. A four-channel spherical-electrode electrostatic induction array then converts the spatially dependent electric-field disturbance into voltage responses through high-impedance signal-conditioning circuits. Because the proposed method uses relative features rather than arrival-time differences, the preprocessing block emphasizes robust event detection, common onset alignment, baseline correction, and fixed-window feature extraction rather than channel-dependent time-delay estimation.

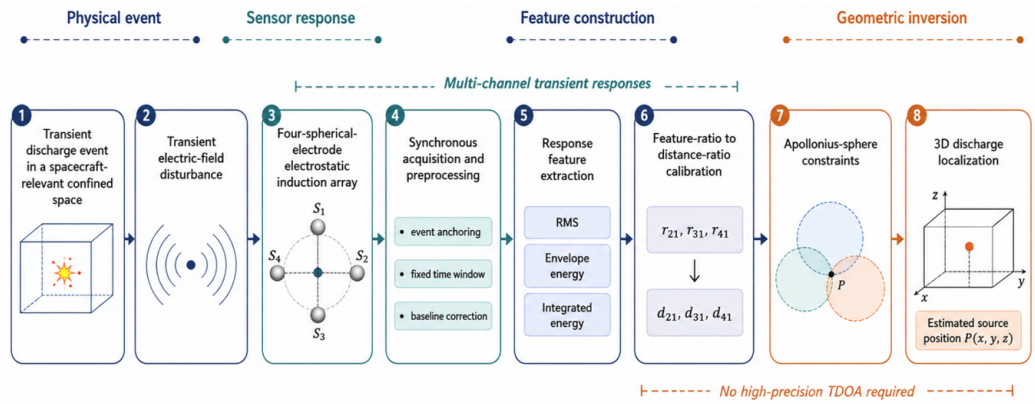


Figure 1. Overall system and method framework for electrostatic-induction-array-based discharge localization. The figure defines four stages: physical event generation, four-channel electrostatic-induction sensing and preprocessing, feature-ratio construction with Power + offset calibration, and Apollonius-sphere-based three-dimensional inversion. RMS denotes root-mean-square value. The distance ratios d_{21}, d_{31}, and d_{41} are estimated from calibrated feature ratios relative to sensor 1. The dashed note indicates that high-precision TDOA estimation is not required.

The feature-construction block converts the four transient responses into root-mean-square (RMS), envelope-energy, and integrated-energy representations and then forms

feature ratios relative to a reference sensor. During calibration, these feature ratios are paired with the known geometric distance ratios of calibration positions and fitted by a compact Power + offset mapping. The geometric-inversion block converts the calibrated distance ratios into Apollonius-sphere constraints and estimates the discharge coordinate by nonlinear residual minimization. Thus, the workflow consists of four explicitly defined stages: physical event generation, multi-channel electrostatic-induction sensing, feature-ratio calibration, and three-dimensional coordinate inversion. The dashed indication in Figure 1 emphasizes that high-precision TDOA estimation is not required in the present framework.

3. Materials and Methods

This section describes the sensing principle, feature construction, calibration mapping, and geometric inversion procedure used in the proposed localization framework. It also clarifies the environmental factors that can affect the model and the boundaries within which the present calibration-based method should be interpreted. The experimental platform and validation design are reported separately in Section 4.

3.1. Electrostatic Induction Response of a Spherical-Electrode Array

A transient discharge event produces a rapid local electric-field disturbance. When a metallic sensing electrode is placed in such a field, the free charge on the electrode surface redistributes according to the external normal electric-field component, following the basic electrostatic-boundary principles of conductors in external fields [28,29]. For an effective sensing area A_e, the induced charge can be written in simplified form as follows:

$$Q_k(t) \approx \varepsilon A_e E_{n,k}(t), \tag{1}$$

where $Q_k(t)$ is the induced charge on the kth electrode, ε is the permittivity of the surrounding medium, and $E_{n,k}(t)$ is the normal component of the external electric field at the electrode. The corresponding induced current is:

$$i_k(t) = \frac{dQ_k(t)}{dt} \approx \varepsilon A_e \frac{dE_{n,k}(t)}{dt}. \tag{2}$$

Thus, an electrostatic induction electrode responds strongly to fast electric-field variations, which is consistent with the pulse-like nature of discharge events and with classical induced-current interpretations for moving or time-varying charge distributions [30,31].

For the localization problem, the detailed source physics can be simplified at the observation scale. Point-charge, electric-dipole, and pulsed-current equivalent models have different distance attenuation laws, but they share a common structure: the sensor response is determined by a source time function and a location-dependent spatial coupling factor [28,29]. Therefore, the measured voltage of the kth channel is expressed as follows:

$$u_k(t) = G_k A_k(\mathbf{p}) s(t) + n_k(t), \tag{3}$$

where G_k is the equivalent gain of the kth sensor and conditioning channel, $A_k(\mathbf{p})$ is the spatial coupling coefficient determined by the discharge position $\mathbf{p}$, the sensor position, and local boundary conditions, $s(t)$ is the common source waveform for the same discharge event, and $n_k(t)$ denotes measurement noise and unmodeled coupling terms. Equation (3) indicates that the useful position information is embedded in the relative differences among channels rather than in the absolute waveform of a single channel.

3.2. Influence of Space Environmental Factors and Applicability Boundaries

Equation (3) is a compact observation model for the calibrated localization problem. Its parameters are not universal constants: the spatial coupling coefficient $A_k(\mathbf{p})$, the equivalent gain G_k, and the unmodeled term $n_k(t)$ can be affected by the surrounding environment and by local spacecraft structures. This point is critical for interpreting the present study. The method proposed here is calibration-based; therefore, its validity depends on whether the calibration geometry and environmental conditions are representative of the application scenario.

Vacuum conditions mainly affect the discharge-formation mechanism and the availability of acoustic propagation paths rather than the quasi-static electrostatic boundary relation itself. In a vacuum or rarefied environment, the discharge path, pulse duration, released charge, and electromagnetic coupling route may differ from those of a needle–plate discharge in air. The proposed feature-ratio method can reduce sensitivity to event-to-event source-strength variation, but it cannot remove environmental changes that alter the spatial coupling functions $A_k(\mathbf{p})$. Therefore, a calibration obtained in ambient air should not be transferred directly to an actual spacecraft configuration without environment-specific recalibration.

Surrounding charged particles and plasma can also influence localization. Ambient plasma may modify spacecraft surface potentials, introduce sheath effects, and screen or redistribute electric fields around surfaces. These effects may change both the baseline electric-field state and the transient coupling path between a discharge source and the sensing electrodes. In addition, spacecraft surfaces, dielectric materials, solar-array interfaces, cable harnesses, and metallic compartments can introduce local boundary coupling, reflections, shielding, and parasitic capacitances. Such boundary effects are precisely why the present method uses empirical feature-ratio calibration rather than a purely analytical free-space attenuation law; however, the calibration must be repeated or updated for each representative structural configuration.

Large temperature differences and thermal cycling can influence both the discharge source and the measurement chain. Temperature-dependent dielectric properties, leakage paths, cable impedance, amplifier bias drift, and mechanical deformation may change the measured feature ratios. For deployment-oriented applications, the sensor array should therefore be calibrated or compensated over the expected thermal range, and the uncertainty budget should include temperature-induced gain drift, sensor-coordinate uncertainty, and residual calibration error.

Consequently, the results of this study should be interpreted as a controlled laboratory verification of the sensing–calibration–inversion chain. They support the feasibility of using relative electrostatic-induction features for confined-space discharge localization, but they do not establish direct on-orbit accuracy. A spacecraft-specific implementation would require calibration and validation in representative metallic/dielectric structures and, ultimately, in thermal-vacuum and plasma conditions.

3.3. Feature-Ratio Construction for Transient Discharge Responses

Direct use of absolute amplitude is not robust for spacecraft-relevant discharge localization. The released charge, discharge path, waveform duration, and front-end coupling may vary from event to event. In addition, fixed differences in sensor mounting, shielding, and analog gain introduce channel-dependent biases. To reduce these effects, this study uses relative features computed from a common analysis window.

Let $x_k[n]$ be the preprocessed discrete signal of the kth sensor in the event window, where $n = 1, 2, \ldots, N$, and let Δt be the sampling interval. Three windowed response representations are considered:

$$F_k^{\mathrm{RMS}} = \sqrt{\frac{1}{N}\sum_{n=1}^{N} x_k^2[n]}, \tag{4}$$

$$F_k^{\mathrm{ENV}} = \Delta t \sum_{n=1}^{N} |\mathcal{A}\{x_k[n]\}|^2, \tag{5}$$

$$F_k^{\mathrm{INT}} = \Delta t \sum_{n=1}^{N} x_k^2[n], \tag{6}$$

where $\mathcal{A}\{\cdot\}$ denotes the analytic signal obtained through the Hilbert transform, and $|\mathcal{A}\{x_k[n]\}|$ is its envelope. The RMS representation describes the overall signal level, the integrated energy represents the total squared-amplitude accumulation in the event window, and the envelope energy emphasizes a smoothed transient-energy envelope. Because all four channels are sampled with the same Δt, this constant factor cancels when energy-type feature ratios are constructed. Therefore, the numerical implementation may omit Δt without changing any feature-ratio values.

It should be noted that the three quantities are not treated as fully independent physical observables. Under a fixed analysis window length and sampling interval, the integrated energy satisfies $F_k^{\mathrm{INT}} = N\Delta t\left(F_k^{\mathrm{RMS}}\right)^2$; consequently, its ratio is a squared scaling of the RMS ratio. It is retained in this study as an alternative nonlinear scaling of the same windowed response energy, allowing the calibration procedure to test whether amplitude-equivalent or energy-scale ratios produce more stable distance-ratio estimates. The envelope-energy representation is also energy-related, but it is computed from the analytic envelope and is used to assess whether a smoothed transient-energy description is more robust to high-frequency ringing, small window shifts, and local waveform distortion.

Taking sensor 1 as the reference, the feature ratio for sensor k is defined as follows:

$$R_{k1}^{(F)} = \frac{F_k}{F_1}, \quad k = 2, 3, 4, \tag{7}$$

where F denotes one of the selected response representations. In this study, the raw ratio F_k/F_1 is used consistently for RMS, envelope energy, and integrated energy. No square-root normalization is applied to the energy-type ratios, because the comparison intentionally preserves the distinction between amplitude-equivalent scaling and energy-scale sensitivity before empirical calibration. The corresponding distance ratio is defined as follows:

$$d_{k1} = \frac{\|\mathbf{p} - \mathbf{s}_k\|}{\|\mathbf{p} - \mathbf{s}_1\|}, \quad k = 2, 3, 4, \tag{8}$$

where $\mathbf{s}_k$ is the known coordinate of the kth sensor. The feature-ratio–distance-ratio model is then calibrated experimentally as follows:

$$d_{k1} = f\left(R_{k1}^{(F)}; \boldsymbol{\theta}\right), \tag{9}$$

where $\boldsymbol{\theta}$ denotes the fitted model parameters. This calibration absorbs the combined influence of sensor geometry, near-field coupling, and fixed-boundary effects into an empirical but physically interpretable mapping.

3.4. Apollonius-Sphere Constraints and Three-Dimensional Inversion

Each estimated distance ratio defines an Apollonius surface, a geometry also closely related to ratio-based and received-signal-strength-difference source-localization formulations used in sensor networks and passive emitter localization [18–21]:

$$\frac{\|\mathbf{p}-\mathbf{s}_k\|}{\|\mathbf{p}-\mathbf{s}_1\|} = d_{k1}, \quad k = 2,3,4. \tag{10}$$

When $d_{k1} \neq 1$, Equation (10) corresponds to a sphere. Its center $\mathbf{c}_{k1}$ and radius r_{k1} are:

$$\mathbf{c}_{k1} = \frac{\mathbf{s}_k - d_{k1}^2 \mathbf{s}_1}{1-d_{k1}^2}, \tag{11}$$

$$r_{k1} = \frac{d_{k1}\|\mathbf{s}_k - \mathbf{s}_1\|}{|1-d_{k1}^2|}. \tag{12}$$

For four non-coplanar sensors, the three independent constraints Ω_{21}, Ω_{31}, and Ω_{41} ideally intersect at the discharge position. In the presence of noise and calibration errors, the three spheres do not strictly intersect at a single point. In addition, when an estimated ratio approaches unity, the corresponding Apollonius surface becomes weakly curved and its explicit sphere representation is numerically less informative. The localization problem is therefore solved directly through distance-ratio residual minimization rather than by explicit geometric intersection:

$$\hat{\mathbf{p}} = \arg\min_{\mathbf{p}\in\mathcal{D}} \sum_{k=2}^{4} \left(\frac{\|\mathbf{p}-\mathbf{s}_k\|}{\|\mathbf{p}-\mathbf{s}_1\|} - \hat{d}_{k1} \right)^2, \tag{13}$$

where $\hat{d}_{k1}$ is the distance ratio estimated from the calibrated feature-ratio model, and $\mathcal{D}$ is the bounded localization domain. In this study, a coarse-grid initialization followed by Levenberg–Marquardt local optimization is used. This strategy combines global stability with efficient local convergence for the low-dimensional inversion problem. The corresponding Apollonius-sphere geometry is illustrated in Figure 2.

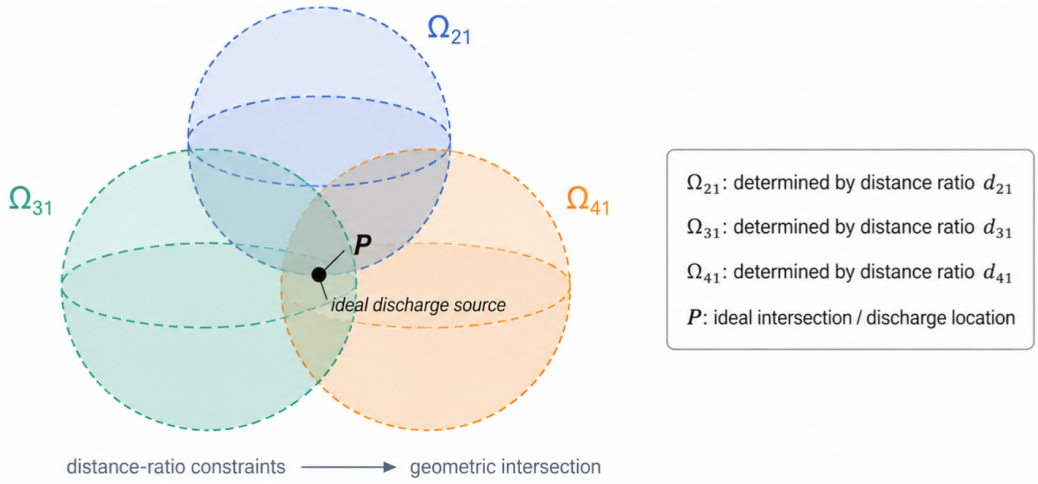


Figure 2. Schematic illustration of the Apollonius-sphere localization principle. Three independent distance-ratio constraints, d_{21}, d_{31}, and d_{41}, define the corresponding Apollonius spheres Ω_{21}, Ω_{31}, and Ω_{41}. Their ideal intersection gives the discharge position P, while in noisy cases, the final coordinate is obtained by nonlinear residual minimization.

4. Experimental Setup and Validation Design

4.1. Experimental Scope and Spacecraft Relevance

The experimental platform in this study is designed to provide a controllable, repeatable, and geometrically known environment for evaluating the proposed sensing–calibration–localization chain. The validation focuses on the engineering process required for discharge localization: localized transient excitation, rapid external electric-field disturbance, multi-channel electrostatic-induction response acquisition, feature-ratio construction, distance-ratio calibration, and three-dimensional inversion.

This experimental scope is consistent with the development pathway of spacecraft sensing and diagnostic technologies, which are commonly assessed first using controlled ground test platforms before being extended to more complex spacecraft environments. The needle–plate source provides a repeatable transient electric-field excitation, while the cubic platform supplies a known confined-space geometry for evaluating the localization algorithm. Although the source formation mechanism and environmental conditions are simpler than those of an operational spacecraft, the experiment captures the measurement-level problem addressed in this work: whether a compact electrostatic-induction array can acquire spatially dependent transient responses and convert them into three-dimensional source-location estimates.

4.2. Laboratory Confined-Space Validation Volume

The experimental domain is a cube with an effective side length of 1 m. This volume is used as a controlled three-dimensional laboratory validation domain rather than as a one-to-one physical model of a specific CubeSat. Representative small-spacecraft dimensions are listed in Table 1 only to provide scale context [32–34]. A 1U CubeSat is much smaller than the present domain, and even 6U–24U CubeSat configurations would require different sensor placement, installation constraints, calibration positions, and boundary models. Therefore, the present 1 m^3 results should not be interpreted as a direct performance estimate for all CubeSat sizes.

Table 1. Representative small-spacecraft dimensions and the laboratory validation domain. The table is provided for scale context only; the 1 m^3 platform is not treated as a direct geometric model of a 1U, 3U, or 6U CubeSat. Values are approximate external dimensions.

Platform	Length (m)	Width (m)	Height (m)
1U CubeSat	0.10	0.10	0.11
3U CubeSat	0.34	0.10	0.10
6U CubeSat	0.34	0.20	0.10
PROBA-class microsatellite	0.60	0.60	0.80
This laboratory validation platform	1.00	1.00	1.00

The 1 m side length was selected for three practical reasons. First, it provides sufficient geometric diversity in source–sensor distance ratios to evaluate the feature-ratio–distance-ratio mapping and the stability of the three-dimensional inversion. Second, the volume is large enough to place a repeatable needle–plate source, four sensing electrodes, and support structures while maintaining known coordinates and avoiding near-contact saturation of the front-end circuit. Third, it provides a conservative ground-test domain for verifying the complete sensing–calibration–localization chain before reducing the array scale for more compact spacecraft compartments. For a practical CubeSat or microsatellite implementation, the localization domain, sensor spacing, calibration grid, and feature-ratio mapping must be redesigned for the actual spacecraft geometry.

The coordinate origin is defined at the center of the cube, and the bounded localization domain used in the present laboratory validation is:

$$-0.5\ \text{m} \leq x, y, z \leq 0.5\ \text{m}. \tag{14}$$

4.3. Discharge Source and Sensor Array

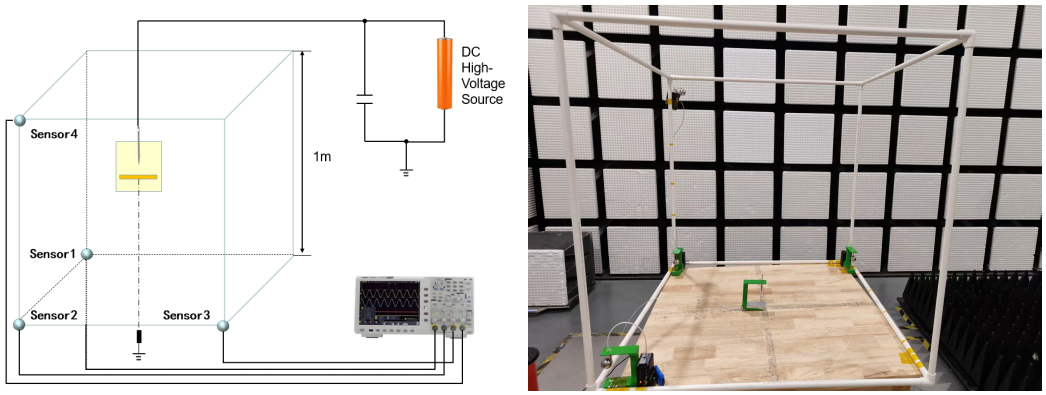
A needle–plate discharge source is used to generate localized transient discharge events. The source consists of a DC high-voltage supply, a CB81 film storage capacitor, and a needle–plate electrode pair. The nominal charging voltage is 4 kV, and the storage capacitance is 10,000 pF. The needle tip radius is approximately 0.1 mm, and the needle–plate spacing is set to 1 mm. This configuration concentrates the high-field region near the needle tip, improves the spatial repeatability of the discharge origin, and provides repeatable transient electric-field disturbances for validating the array localization framework.

The sensing array consists of four polished spherical electrostatic induction electrodes with a diameter of 2 cm. The electrodes are arranged at four non-coplanar vertices of the cubic domain to improve three-dimensional observability and avoid degeneracy in the distance-ratio constraints. The coordinate origin is located at the center of the 1 m^3 cube. The sensor-center coordinates used in both calibration and localization are:

$$\begin{aligned} \mathbf{s}_1 &= (0.5, -0.5, -0.5)\ \text{m}, & \mathbf{s}_2 &= (-0.5, -0.5, -0.5)\ \text{m}, \\ \mathbf{s}_3 &= (-0.5, 0.5, -0.5)\ \text{m}, & \mathbf{s}_4 &= (-0.5, -0.5, 0.5)\ \text{m}. \end{aligned} \tag{15}$$

This geometry provides three independent distance-ratio constraints relative to sensor 1 and ensures that the four sensing points are non-coplanar.

The experimental platform and the corresponding laboratory scene are shown in Figure 3. The schematic panel clarifies the relative positions of the cubic frame, four spherical sensors, the needle–plate discharge structure, the high-voltage source, the grounding path, and the oscilloscope. The photograph further shows the physical 1 m^3 frame, the sensor supports, and the discharge-source arrangement used in the validation experiment.



(**a**) Experimental setup schematic (**b**) Actual experimental scene

Figure 3. Experimental platform for validating the proposed localization framework. (**a**) Schematic arrangement of the 1 m^3 confined-space platform, four electrostatic induction sensors, needle–plate discharge source, high-voltage source, grounding path, and acquisition system. (**b**) Actual laboratory scene of the confined-space validation platform, showing the physical frame, sensor supports, and discharge-source arrangement.

4.4. Signal Conditioning, Acquisition, and Sensor Consistency

The induced signal generated by a spherical electrode is weak, transient, and associated with a high source impedance. For spacecraft-oriented instrumentation, such sensing circuits must also be considered together with electrical-interface and electromagnetic-

compatibility constraints [35,36]. The signal-conditioning chain therefore includes a high-input-impedance front-end stage, AC coupling for baseline stabilization, and a secondary voltage-amplification stage. In the prototype system, an INA116 instrumentation amplifier is used for high-impedance buffering and differential extraction, with a first-stage gain of approximately 3.5. The INA116 output is AC-coupled through a 1 nF capacitor and a 2 MΩ resistor to suppress DC offset and low-frequency drift. An OPA4277 precision operational amplifier is then used for secondary non-inverting voltage amplification with a gain of approximately 11, giving an overall voltage gain of about 38.5. The acquisition system samples the four channels synchronously at 1.25 GSa/s.

Before localization experiments, channel consistency is evaluated by injecting a 100 kHz, 1 V peak-to-peak sine signal into the four channels under identical test conditions. The measured output peak-to-peak values are 220.84 mV, 216.62 mV, 216.77 mV, and 218.37 mV. The relative standard deviation is approximately 0.90%, indicating that the fixed amplitude inconsistency among channels is small compared with the discharge-induced spatial response differences.

Table 2 summarizes the engineering specifications that can be clearly identified from the current laboratory prototype. The present setup includes bench-top high-voltage and acquisition instruments; therefore, the mass and power consumption of the complete experimental setup are not representative of a miniaturized onboard spacecraft unit. To avoid overstating deployment readiness, the engineering interpretation in this paper is limited to the compact sensing principle and to the feasibility of the calibration-based localization chain. A practical spacecraft-oriented implementation would require miniaturized low-power front-end electronics, an integrated acquisition unit, radiation and thermal design, electromagnetic-compatibility verification, and mission-specific environmental validation.

Table 2. Engineering specifications and deployment-related interpretation of the current prototype. Values describe the laboratory validation system unless otherwise noted.

Item	Current Prototype Value	Deployment-Related Interpretation
Sensing element	Four polished spherical electrodes, 2 cm diameter each	The sensing heads are compact and structurally simple; spacecraft integration still requires packaging, insulation, and mounting design.
Array geometry	Four non-coplanar sensing positions over the 1 m^3 laboratory domain	The geometry is selected for observability in the laboratory platform; practical spacecraft arrays must be scaled and recalibrated for the actual compartment.
Signal conditioning	INA116 high-input-impedance front end, AC coupling, OPA4277 secondary amplification, total voltage gain about 38.5	Demonstrates the required high-impedance transient sensing chain; component selection and power optimization remain necessary for an onboard spacecraft implementation.
Acquisition	Synchronous four-channel acquisition at 1.25 GSa/s using external laboratory instrumentation	Supports algorithm verification; an onboard unit would require a compact digitizer or event-driven transient recorder.

Table 2. *Cont.*

Item	Current Prototype Value	Deployment-Related Interpretation
Power consumption	Not quantified for a miniaturized onboard unit in the present study	The present external instruments dominate system power and are not representative of an integrated spacecraft-oriented electronics module.
Mass and package size	Not quantified for a packaged onboard module in the present study	The mechanical frame and external instruments are for ground validation only; future work should quantify the packaged sensor module and acquisition electronics.

4.5. Event Detection, Onset Determination, and Baseline Correction

The transient response contains a rapidly varying oscillatory waveform. If the maximum derivative sample is directly used as the event anchor, the anchor may fall inside the already developed discharge response rather than at the physical onset. In that case, a pre-anchor baseline window may contain early discharge components and bias the subsequent energy features. To avoid this problem, a robust two-stage preprocessing procedure is adopted. The derivative maximum is used only for coarse event localization, whereas the final feature window is aligned to a separately detected discharge onset.

First, a coarse event index is obtained from the four-channel joint derivative energy:

$$E_{\Delta}[n] = \sum_{k=1}^{4} (x_k[n] - x_k[n-1])^2, \tag{16}$$

and

$$n_{\text{peak}} = \arg\max_{n} E_{\Delta}[n]. \tag{17}$$

Here, n_{peak} denotes the sample with the strongest multi-channel derivative response. It is not regarded as the discharge onset, but only as a coarse indicator of the event region.

Second, a quiet pre-event segment is automatically selected before n_{peak} to estimate the local background level. In the implementation used in this study, a 100-sample sliding window is searched within the interval from $n_{\text{peak}} - 450$ to $n_{\text{peak}} - 20$. The selected quiet segment minimizes a combined amplitude- and derivative-variation score. For the kth channel, the background mean μ_k, the robust amplitude scale σ_k, and the robust derivative scale $\sigma_{\Delta,k}$ are estimated from this quiet segment using the median absolute deviation when applicable. At a sampling rate of 1.25 GSa/s, the 450-sample backward search length, 20-sample exclusion interval, and 100-sample quiet window correspond to approximately 360 ns, 16 ns, and 80 ns, respectively.

Third, normalized multi-channel amplitude and derivative activities are constructed as follows:

$$A[n] = \frac{1}{4} \sum_{k=1}^{4} \left(\frac{x_k[n] - \mu_k}{\sigma_k} \right)^2, \tag{18}$$

$$D[n] = \frac{1}{4} \sum_{k=1}^{4} \left(\frac{x_k[n] - x_k[n-1]}{\sigma_{\Delta,k}} \right)^2. \tag{19}$$

The corresponding activity thresholds are defined as the larger value between a robust threshold estimated from the quiet-segment activity and a dimensionless lower bound of 4 for the normalized activity score:

$$T_A = \max\{\text{median}(A_Q) + 6\,\text{MAD}(A_Q),\ 4\}, \tag{20}$$

$$T_D = \max\{\text{median}(D_Q) + 6\,\text{MAD}(D_Q),\ 4\}, \tag{21}$$

where A_Q and D_Q denote the amplitude and derivative activities in the selected quiet segment. The lower bound of 4 is not a voltage threshold; it is an empirical normalized-activity floor used to avoid unrealistically low thresholds when the quiet segment has very small fluctuations. A combined activity score is then calculated as follows:

$$S[n] = \max\left(\frac{A[n]}{T_A}, \frac{D[n]}{T_D}\right). \tag{22}$$

A sample is considered active when $S[n] > 1$.

Finally, the discharge onset n_{onset} is obtained by a backward search before n_{peak}. The first sample is selected when the activity remains above the threshold for five consecutive samples, while the preceding 30 samples contain no more than two active samples. This rule suppresses occasional noise-triggered crossings and provides a common onset for all four channels. Because the proposed method uses feature ratios rather than arrival-time differences, a unified multi-channel onset is used for all sensors to avoid introducing artificial channel-dependent window shifts.

Baseline correction and feature extraction are then performed with respect to n_{onset}. The baseline mean is computed from a 100-sample segment ending five samples before the detected onset:

$$\mathcal{B} = \left[n_{\text{onset}} - N_{\text{gap}} - N_{\text{base}},\ n_{\text{onset}} - N_{\text{gap}} - 1\right], \tag{23}$$

where $N_{\text{base}} = 100$ and $N_{\text{gap}} = 5$, corresponding to approximately 80 ns and 4 ns, respectively. After channel-wise baseline subtraction, the feature window is defined as follows:

$$\mathcal{W} = [n_{\text{onset}},\ n_{\text{onset}} + N_{\text{feat}} - 1], \tag{24}$$

where $N_{\text{feat}} = 150$, corresponding to approximately 120 ns. RMS, envelope energy, and integrated energy are calculated within this common onset-aligned window. This preprocessing strategy prevents early discharge oscillations from entering the baseline estimate and preserves a consistent time support for the feature-ratio calculation. The key experimental, acquisition, and signal-processing parameters are summarized in Table 3.

Table 3. Key experimental, acquisition, and signal-processing parameters of the prototype system.

Category	Parameter	Value and Role
Experimental system	Domain size	1 m × 1 m × 1 m confined-space platform
	Discharge source	Needle–plate transient source, charged at 4 kV with a 10,000 pF storage capacitor
	Source geometry	Needle tip radius of approximately 0.1 mm and needle–plate spacing of 1 mm
	Sensor array	Four spherical induction electrodes with 2 cm diameter, arranged at non-coplanar vertices
Acquisition chain	Signal conditioning	High-input-impedance buffering, AC coupling, and secondary voltage amplification
	Sampling rate	1.25 GSa/s synchronous four-channel acquisition

Table 3. *Cont.*

Category	Parameter	Value and Role
Signal processing	Coarse event localization	Maximum of four-channel joint derivative energy
	Onset detection	450-sample backward search, 100-sample quiet window, 20-sample pre-peak exclusion, and robust MAD-based activity threshold
	Onset criterion	Five consecutive active samples after a 30-sample quiet check with at most two active samples
	Baseline and feature windows	100-sample baseline segment with a 5-sample protection gap; 150-sample onset-aligned feature window

4.6. Calibration and Localization Test Design

4.6.1. Calibration Experiment Design

A calibration experiment is conducted before unknown-position localization. Forty known discharge positions are selected in the 1 m^3 domain to cover the usable localization volume, including both interior and near-boundary regions, and to provide diverse source–sensor distance-ratio combinations. The positions are not concentrated around any single sensor. Locations extremely close to a sensing electrode are intentionally excluded, because such configurations can drive the front-end response toward saturation and no longer represent the intended linear or quasi-linear feature-ratio calibration regime. The calibration set therefore prioritizes broad spatial coverage within the unsaturated measurement range rather than including physically possible but diagnostically uninformative near-contact discharge cases. At each position, the needle–plate source is triggered under the same nominal voltage and the four-channel transient responses are recorded synchronously. For each event, preprocessing is applied, the selected response representations are extracted, and the feature ratios relative to sensor 1 are computed. The true geometric distances from the discharge position to the sensor centers in Equation (15) are calculated from the known coordinates, giving the corresponding distance ratios.

The calibration dataset therefore contains paired samples of the following form:

$$\left\{R_{k1}^{(F)}, d_{k1}\right\}, \quad k = 2, 3, 4, \tag{25}$$

for each known discharge position and each selected feature. Thus, the 40 calibration positions provide three independent ratio–distance pairs relative to sensor 1 for each response representation. These experimentally obtained ratio–distance samples are used to fit the feature-ratio–distance-ratio mapping in Equation (9). The fitted curves reported for the experimental panels in the subsequent fitting results therefore represent the experimental calibration-data trend for each response representation.

4.6.2. COMSOL-Assisted Spatial Response Analysis

A COMSOL electrostatics model is used as an auxiliary tool to examine the spatial continuity of the response-ratio relation under the same geometric configuration. The model is implemented in COMSOL Multiphysics 6.2 using the Electrostatics interface of the AC/DC module. It includes the four spherical electrodes at the same coordinates as the experiment, the needle–plate source assembly, and an expanded surrounding air domain. To reduce artificial truncation effects from the external boundary, the effective 1 m^3 observation domain is embedded in a spherical air domain with a radius of 1.5 m. The air relative permittivity is set to 1, and the needle, plate, and spherical sensing electrodes are treated as highly conducting metal domains represented by aluminum material.

The needle electrode is assigned a 4 kV potential, while the plate electrode is grounded. The spherical sensing electrodes are treated as conducting domains, and their surface-charge responses are used for relative electrostatic-coupling comparison rather than for absolute charge output prediction. The needle–plate assembly is moved as a rigid source structure during the parametric position scan so that the local high-field geometry remains consistent with the experimental discharge source. The center coordinate of the source assembly is scanned within the cube-centered domain:

$$x, y, z \in [-0.5, 0.5] \text{ m}, \tag{26}$$

with a uniform scan interval of $\Delta x = \Delta y = \Delta z = 0.1$ m, corresponding to a regular grid of $11 \times 11 \times 11 = 1331$ candidate source-center locations over the validation volume. This 0.1 m interval is used to sample the dominant spatial trend of the electrostatic response–ratio relation rather than to construct a high-resolution localization lookup table. The electrostatic problem was solved in the quasi-static configuration for each sampled source position in batch form, and the induced-charge ratios were stored for subsequent fitting and visualization. The mesh is refined around the needle tip, the needle–plate gap, and the spherical-electrode surfaces, while a coarser mesh is used in the far air domain to balance field-resolution accuracy and computational cost. For each scanned source position, the surface charge density on each spherical electrode is integrated over the electrode boundary to obtain the total induced charge. The four induced-charge responses are then converted into relative response quantities and processed using the same feature-ratio construction as the experimental data.

Figure 4 shows a representative COMSOL electrostatic-potential distribution obtained for one sampled source position. The result illustrates the strong potential concentration near the needle–plate source and the rapid spatial attenuation of the electrostatic field in the surrounding air domain. This field distribution provides a qualitative visualization of the near-field coupling environment from which the sensing-electrode induced-charge ratios are extracted.

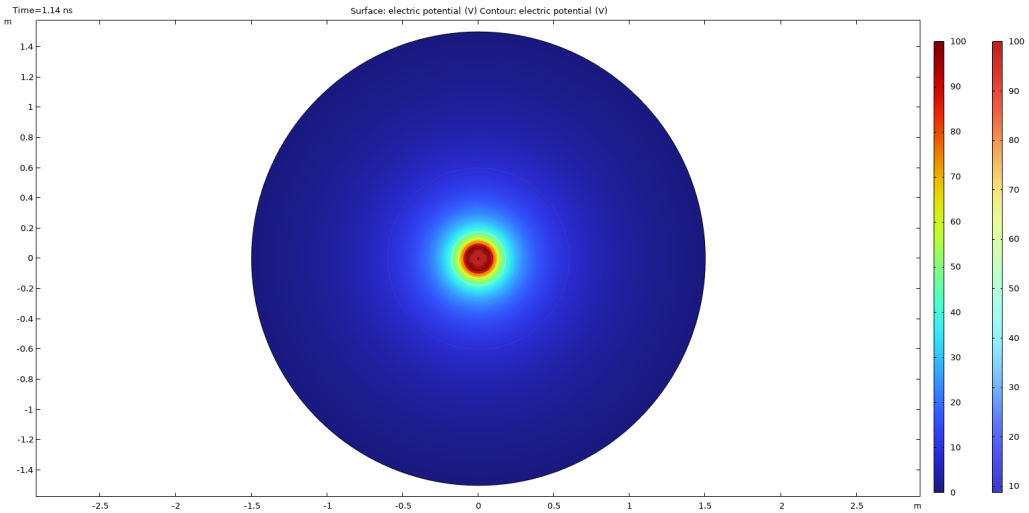


Figure 4. Representative COMSOL electrostatic-potential distribution for one sampled needle–plate source position. The potential is concentrated near the source region and decays over the surrounding computational air domain. This result is used as a qualitative visualization of the electrostatic coupling field in the auxiliary simulation rather than as a direct transient plasma-discharge waveform.

The simulation is used to examine the spatial structure of the electrostatic coupling relation under the same array geometry and boundary configuration as the experiment. Its role is to support the interpretation of the response–ratio trend and to provide auxiliary

electrostatic response samples for fitting and visualization. It is not used as a transient plasma-discharge waveform model.

4.6.3. Model Fitting and Feature Selection

Three response representations are compared: RMS, envelope energy, and integrated energy. This comparison is not intended to imply that all three features are mutually independent physical measurements. RMS and integrated energy are mathematically linked under a fixed window, while envelope energy provides a smoothed energy-envelope representation of the same transient response. They are compared as alternative feature scalings for the empirical feature-ratio–distance-ratio calibration. For each representation, the training samples are formed by pairing the measured feature ratios with the corresponding geometric distance ratios. The candidate functions are restricted to compact monotonic mappings that can be interpreted as empirical attenuation laws, including a pure power law, a power law with an additive offset, single-exponential and double-exponential forms, and a reciprocal-type mapping. Model selection is not based on visual curve agreement alone. Instead, the fitting residual, coefficient of determination, model complexity, and corrected Akaike information criterion (AICc) are considered together. For a model with k fitted parameters and n samples, AICc is calculated as follows:

$$\mathrm{AICc} = n \ln\left(\frac{\mathrm{SSE}}{n}\right) + 2k + \frac{2k(k+1)}{n-k-1}, \tag{27}$$

where SSE is the residual sum of squares. A smaller AICc indicates a better balance between fitting accuracy and model parsimony.

The same candidate-model screening strategy is applied to the feature-ratio–distance-ratio datasets before the final calibration form is fixed. A representative comparison using the simulated RMS dataset is included in the Results section to document the model selection rationale in the main text without adding repetitive candidate-model panels. Considering the representative AICc comparison, the observed residual behavior during calibration, the compact three-parameter structure, and the stability of the fitted curves within the bounded domain, the power law with an additive offset, hereafter referred to as the *Power + offset* model, is adopted as the calibration form. Therefore, the calibrated feature-ratio–distance-ratio mapping is written as follows:

$$\hat{d}_{k1}^{(F)} = a_F \left(R_{k1}^{(F)}\right)^{b_F} + c_F, \tag{28}$$

where $R_{k1}^{(F)}$ is the feature ratio for response representation F, $\hat{d}_{k1}^{(F)}$ is the estimated distance ratio, and a_F, b_F, and c_F are the fitted coefficients for that response representation. The additive offset represents the finite asymptotic distance-ratio level in the bounded experimental domain and prevents the mapping from being forced to approach zero at large feature ratios.

Using the *Power + offset* model, the experimental training fits for RMS, envelope energy, and integrated energy give coefficients of determination of $R^2 = 0.9068$, 0.9393, and 0.9081, respectively. These values summarize the calibration quality of the three response representations in the experimental fitting dataset. The envelope-energy representation provides the highest fitting consistency, indicating that the smoothed energy envelope better preserves the stable spatial attenuation trend while reducing sensitivity to high-frequency ringing and local waveform distortion. RMS is computationally simple but more sensitive to the ratio between effective signal duration and background noise within the fixed window. Integrated energy represents a windowed energy-scale form of the RMS response; because

it is proportional to squared RMS for a fixed window, its role in this comparison is to test whether energy-scale nonlinear feature ratios improve or degrade the calibrated mapping.

4.6.4. Independent Localization Test and Evaluation Metrics

After calibration, ten independent discharge positions are used for localization testing. These positions are not used in model fitting. For each test event, the four-channel response is preprocessed, features are extracted, feature ratios are converted into distance ratios, and the nonlinear objective in Equation (13) is minimized to estimate the discharge position.

For a test point with true coordinate $\mathbf{p}_i = [x_i, y_i, z_i]^{\mathrm{T}}$ and estimated coordinate $\hat{\mathbf{p}}_i = [\hat{x}_i, \hat{y}_i, \hat{z}_i]^{\mathrm{T}}$, the three-dimensional localization error is:

$$e_i = \|\hat{\mathbf{p}}_i - \mathbf{p}_i\|_2. \tag{29}$$

The mean three-dimensional error is:

$$\bar{e} = \frac{1}{N_{\mathrm{test}}} \sum_{i=1}^{N_{\mathrm{test}}} e_i. \tag{30}$$

5. Results

5.1. Four-Channel Transient Responses

The four-channel baseline-corrected responses show clear transient waveforms after a localized discharge event. Although the overall waveform is driven by the same source event, the amplitude and energy distribution differ among the four sensors. These spatially dependent differences provide the observation basis for feature-ratio localization. Figure 5 shows a representative processed discharge waveform after robust onset detection, protected pre-onset baseline correction, and onset-aligned feature-window selection.

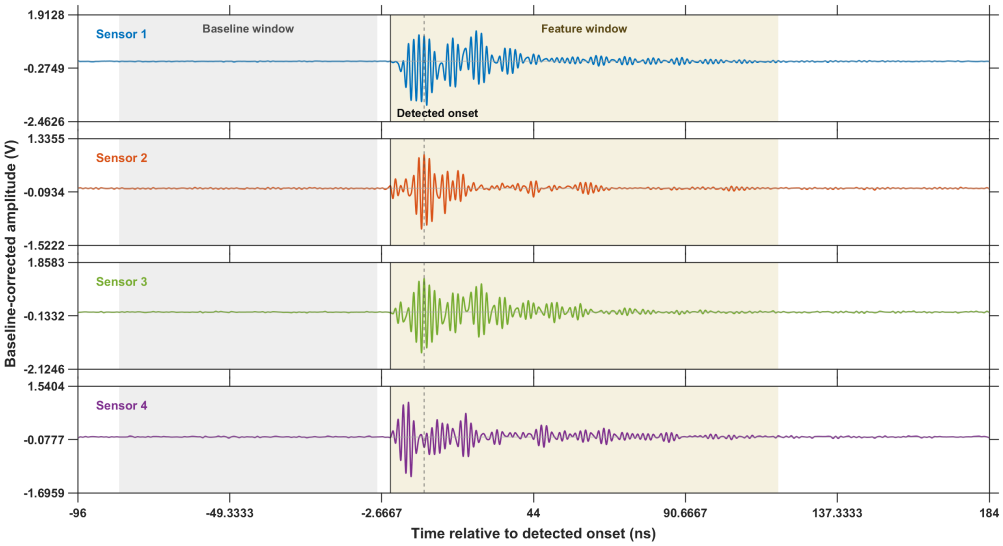


Figure 5. Processed transient discharge signals recorded by the four electrostatic induction sensors after robust onset detection and baseline correction. The protected baseline window, the detected discharge onset n_{onset}, the feature window W, and the derivative-energy peak n_{peak} are indicated in the figure. The derivative-energy peak is used only for coarse event localization, whereas the detected discharge onset defines the start of the common feature window used for feature-ratio calculation.

5.2. Calibration of Feature-Ratio–Distance-Ratio Models

The calibration samples show a stable nonlinear relationship between the feature ratio and the distance ratio. To make the model-selection process explicit while keeping the main text concise, the candidate-model comparison is illustrated using a representative simulated RMS dataset. Five monotonic candidate models are evaluated: pure power law, *Power + offset*, single exponential, double exponential, and reciprocal forms. As shown in Figure 6, the *Power + offset* model achieves the minimum AICc for this representative dataset, maintains a compact three-parameter structure, and shows a low residual level without the excessive complexity of the double-exponential alternative. This representative comparison provides the explicit model selection evidence presented in this manuscript and motivates the subsequent use of the *Power + offset* function as the calibration form.

The dominant mapping structure is consistent across the experimental and COMSOL-assisted fitting results, although the fitted parameters differ because the experimental data include discharge fluctuation, analog-chain nonidealities, and boundary coupling. In Figure 7, the upper panels present the experimental feature-ratio–distance-ratio fitting results for RMS, envelope energy, and integrated energy, while the lower panels present the corresponding simulation-data fitting results. Together, these fittings support the use of an experimentally calibrated *Power + offset* mapping rather than a purely analytical free-space attenuation law.

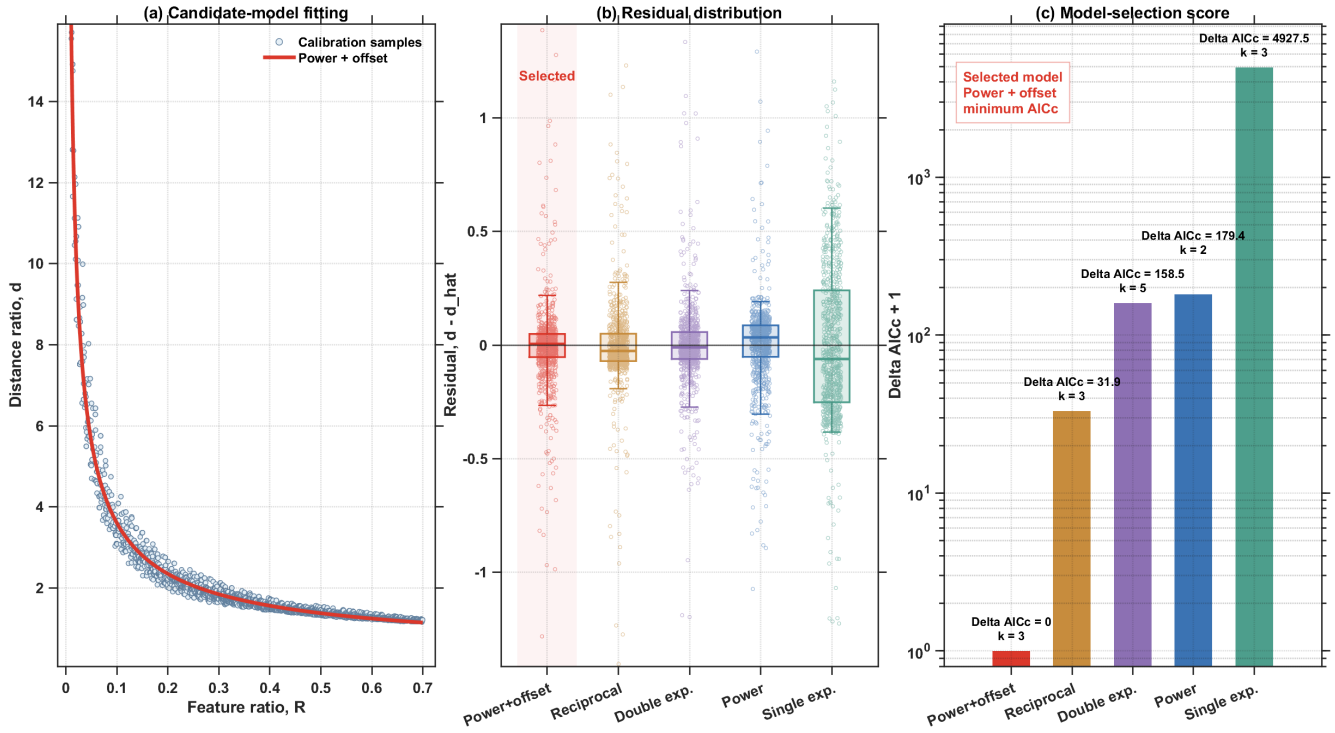


Figure 6. Representative model comparison for selecting the feature-ratio–distance-ratio calibration function using the simulated RMS dataset. Here, R denotes the feature ratio, d denotes the geometric distance ratio, and AICc denotes the corrected Akaike information criterion. (**a**) Fitting curve of the selected *Power + offset* model. (**b**) Residual distributions $d - \hat{d}$ of the evaluated models. (**c**) Model selection scores expressed as $\Delta\text{AICc} + 1$, where the minimum-AICc *Power + offset* model has $\Delta\text{AICc} = 0$. Adding 1 enables logarithmic-scale visualization. This representative result indicates that the selected model provides a favorable balance between fitting accuracy and model complexity.

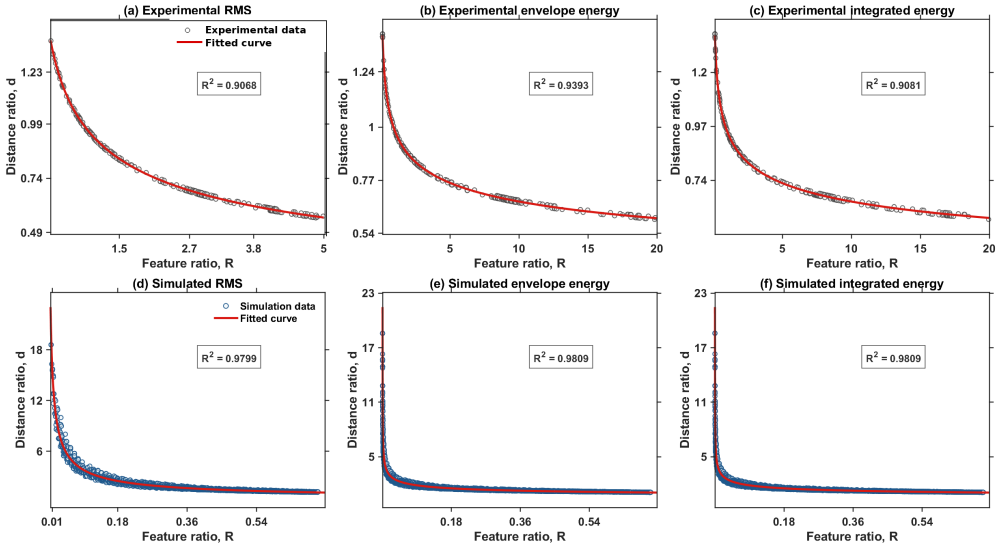


Figure 7. Feature-ratio–distance-ratio fitting results for the RMS, envelope-energy, and integrated-energy features. Solid curves denote the fitted *Power + offset* mapping $\hat{d} = aR^b + c$, where R is the feature ratio and $\hat{d}$ is the estimated distance ratio. In the upper panels, markers denote experimental fitting data; in the lower panels, markers denote simulation samples. The envelope-energy feature provides the highest experimental fitting consistency among the three response representations.

5.3. Localization Accuracy of Independent Test Points

The independent localization test demonstrates that the proposed method can reconstruct discharge positions in the 1 m^3 domain. The distance-ratio estimates used for inversion are obtained from the selected *Power + offset* calibration model for each response representation. Table 4 summarizes the localization performance of three feature choices, where MAE denotes the mean absolute error along each coordinate axis and SD denotes the standard deviation of the three-dimensional error. In addition to the mean three-dimensional error, the median, maximum, and standard deviation of the three-dimensional error are reported to characterize the error distribution over the ten independent test points. The envelope-energy representation provides the lowest mean, median, and maximum three-dimensional errors in the current dataset.

Table 4. Localization performance of three feature models for ten independent test points.

Feature	MAE-x (cm)	MAE-y (cm)	MAE-z (cm)	Mean 3D (cm)	Median 3D (cm)	Max 3D (cm)	SD 3D (cm)
RMS	5.6	2.4	5.2	8.92	8.64	14.70	3.09
Envelope energy	2.2	3.9	4.3	7.01	6.94	10.05	2.67
Integrated energy	5.5	3.4	4.9	8.49	9.38	11.92	2.72

The detailed envelope-energy localization results are listed in Table 5. These values show that the estimated positions generally preserve the correct spatial quadrant and relative distribution of the true test points. Larger errors occur near boundary or high-z regions, where the array geometry and boundary coupling reduce the sensitivity of the distance-ratio constraints.

Figure 8 compares the true discharge positions with the reconstructed positions obtained using the three response representations and summarizes the corresponding three-dimensional localization errors over the ten independent test points. Compared with RMS and integrated energy, the envelope-energy feature reduces the mean three-dimensional localization error by 21.4% and 17.4%, respectively, in the present ten-point test dataset.

Table 5. Envelope-energy localization results for ten independent test points.

No.	True Position (cm)	Estimated Position (cm)	3D Error (cm)
1	(23, −34, −17)	(21, −28, −13)	7.48
2	(−21, 27, 19)	(−26, 28, 17)	5.48
3	(43, 12, −28)	(38, 12, −24)	6.40
4	(−11, −47, 33)	(−13, −38, 29)	10.05
5	(5, 40, 5)	(5, 39, 6)	1.41
6	(−39, −7, −36)	(−37, −2, −33)	6.16
7	(33, 37, 21)	(33, 30, 27)	9.22
8	(−35, 13, −6)	(−31, 14, −3)	5.10
9	(14, −13, 49)	(13, −10, 40)	9.54
10	(−10, −22, −47)	(−9, −16, −40)	9.27

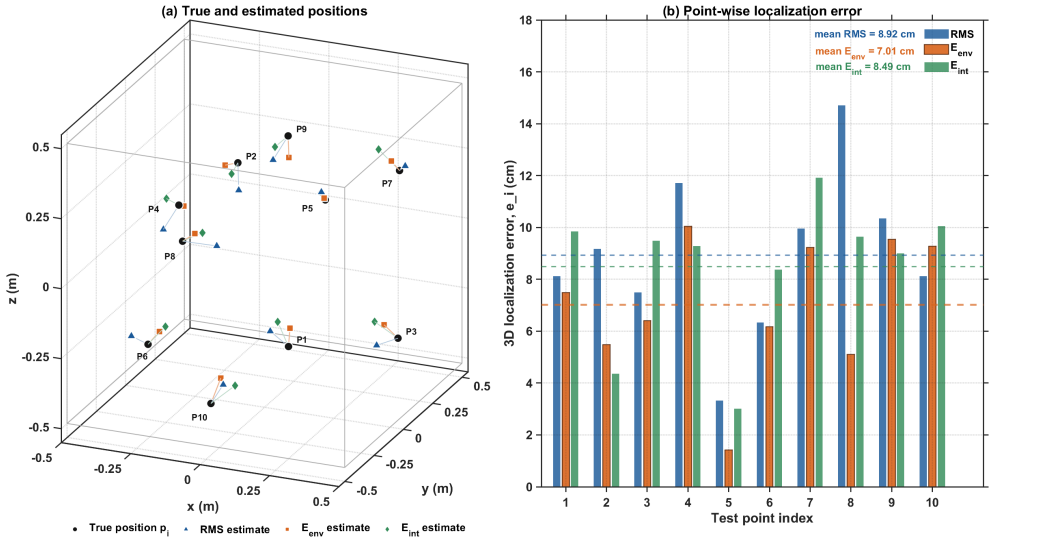


Figure 8. Localization results for the ten discharge test points. (**a**) Three-dimensional comparison between the true discharge positions $\mathbf{p}_i$ and the estimated positions $\hat{\mathbf{p}}_i$ obtained using RMS, envelope energy, and integrated energy. (**b**) Three-dimensional localization error comparison, where $e_i = \|\hat{\mathbf{p}}_i - \mathbf{p}_i\|_2$. The dashed horizontal lines denote the mean localization errors of the corresponding feature groups, and the envelope-energy result is emphasized because it gives the lowest mean three-dimensional localization error in the present test dataset.

5.4. Error Characteristics

The error distribution is not purely random. For boundary points, the estimated coordinates tend to contract toward the interior of the array. This center-contraction trend is more visible for the integrated-energy representation, which preserves an energy-scale version of the RMS response and may amplify the influence of residual ringing and background components in the fixed window. The RMS representation is computationally simple but can be affected by local waveform distortion and the ratio of signal duration to background duration. By contrast, the envelope-energy representation uses the analytic envelope to describe the smoothed transient-energy evolution and is less sensitive to high-frequency oscillation and small window shifts. This explains its better overall performance in the present experiment.

6. Discussion

6.1. Experimental Verification and Methodological Significance

The 1 m^3 confined-space experiment verifies the feasibility of the proposed sensor-to-localization chain under controlled geometry and repeatable transient excitation. The re-

sults indicate that a localized discharge-induced electric-field disturbance can be captured by a four-electrode electrostatic induction array, that relative response features retain spatially dependent information, that feature ratios can be transformed into distance-ratio constraints through calibration, and that the resulting Apollonius-sphere residual problem can recover three-dimensional source coordinates with centimeter-level accuracy in the present laboratory platform.

The experimental results also clarify the role of feature scaling in the localization process. RMS and integrated energy provide amplitude-equivalent and energy-scale descriptions of the same fixed-window response, whereas envelope energy introduces a smoothed representation of the transient energy evolution. Among the evaluated representations, envelope energy provides the most consistent calibration and the lowest localization error. This behavior is physically reasonable because the envelope-based quantity reduces sensitivity to high-frequency ringing while retaining the dominant spatially dependent transient-energy distribution. This suggests that, for electrostatic-induction responses in confined geometries, the spatially informative component is better represented by a smoothed transient-energy envelope than by instantaneous amplitude or window-wide squared accumulation alone.

6.2. Distinction from RSS-Based Apollonius Localization

The proposed method should be distinguished from traditional RSS-based Apollonius localization. In a typical RSS localization problem, the received signal strength is related to source–receiver distance through an assumed or calibrated path-loss law, and the resulting strength ratios are used to construct geometric constraints. In contrast, the present method does not use a communication-style RSS path-loss model or absolute received field strength. The measured quantities are transient electrostatic-induction responses generated by a discharge-induced electric-field disturbance. The input to the localization model is not the raw amplitude of one channel, but the ratio of windowed electrostatic-induction features extracted from synchronized transient responses.

The Apollonius-sphere formulation is therefore used only as the geometric inversion tool after the feature-ratio–distance-ratio relation has been obtained experimentally. The technical contribution lies in combining compact electrostatic-induction sensing, robust onset-aligned feature extraction, empirical feature-ratio calibration, and nonlinear three-dimensional inversion for confined-space discharge localization. This distinction is important because the calibration can absorb fixed channel gain, local boundary coupling, and array geometry within the calibrated domain, whereas a generic free-space RSS attenuation law would be unreliable in confined metallic or dielectric spacecraft-like structures.

6.3. Applicability to Spacecraft Environments and Current Limitations

The present experiment is intended as a spacecraft-oriented preliminary verification of the electrostatic-induction sensing and localization method, not as a complete reproduction of an operational spacecraft environment. It provides a controlled configuration in which source position, sensor geometry, and acquisition conditions are known, making it suitable for evaluating the feature-ratio calibration and inversion procedure. In practical spacecraft applications, however, the local boundary conditions may include metallic cavities, dielectric materials, cable harnesses, plasma interactions, vacuum conditions, radiation exposure, and thermal cycling. These factors may alter electrostatic coupling paths and must be included in subsequent environment-specific calibration and validation.

Several limitations should therefore be emphasized. First, all experimental results in this study were obtained under ambient laboratory conditions using a needle–plate source in air. The discharge-formation mechanism, source waveform, and coupling path may differ

under vacuum, plasma, and spacecraft-material conditions. Second, the 1 m^3 platform is a controlled validation domain rather than a direct geometric analog of a particular CubeSat. A 1U or 6U CubeSat implementation would require a smaller and differently arranged sensor array, a new calibration grid, and a spacecraft-specific boundary model. Third, the current validation uses forty calibration positions and ten independent test positions. This dataset is sufficient for preliminary feasibility verification but not for demonstrating full robustness across all spacecraft structures, discharge types, and environmental states. Fourth, the method is empirical-calibration-dependent: geometry, boundary effects, sensor characteristics, and part of the analog-chain response are absorbed into fitted parameters. This feature is useful for complex confined structures, but it also means that the fitted model should not be transferred outside its calibrated domain without revalidation.

Accordingly, the localization errors reported in this study should be interpreted as performance values for the present experimental geometry and calibration conditions. They demonstrate that the method is feasible as a ground-based sensing–calibration–inversion chain and provide a technical basis for spacecraft-oriented discharge-monitoring research. They do not establish direct on-orbit performance or readiness for spacecraft deployment.

6.4. Engineering Implications for Spacecraft Discharge Monitoring

The proposed method has potential value for spacecraft engineering applications because it combines simple sensing heads with a calibration-based geometric inversion framework. The spherical electrostatic induction electrodes are compact and structurally simple, and the method relies on relative energy features rather than explicit TDOA estimation, thereby reducing the requirement for high-precision arrival-time picking. The feature-ratio calibration can incorporate fixed sensor-gain differences, array geometry, and boundary-coupling effects into an empirical mapping, which is useful when analytical propagation modeling is difficult.

At the same time, the present prototype should not be regarded as a ready-to-deploy onboard system. The laboratory setup uses bench-top high-voltage and acquisition equipment, and the mass, size, and power of the full experimental system are not representative of spacecraft hardware. A deployable version would need miniaturized high-input-impedance front-end electronics, event-triggered transient acquisition, low-power operation, electromagnetic-compatibility design, radiation and thermal assessment, and mechanical packaging compatible with spacecraft integration. Potential applications after such development include discharge source tracing in spacecraft ground qualification tests, localized monitoring near high-voltage solar-array interfaces, dielectric structures, cable harnesses, and other ESD-susceptible regions.

6.5. Comparison with Representative Localization Strategies

Table 6 compares the proposed method with representative discharge localization strategies reported in the partial-discharge, sensor-localization, and received-signal-strength-difference literature [17–21,24]. The proposed approach is not intended to replace established RF, acoustic, optical, or TDOA-based methods. Instead, it provides a complementary option for compact, reduced-timing-dependence confined-space monitoring when a calibrated electrostatic induction array can be installed.

Table 6. Qualitative comparison of representative discharge localization strategies for confined-space spacecraft-oriented monitoring. The proposed method is a calibrated electrostatic-induction feature-ratio method rather than a conventional absolute RSS localization method.

Method	Strength	Key Limitation
TDOA	Direct geometric interpretation	Requires accurate timing, high sampling rate, and known propagation velocity
RF/UHF/HFCT	Sensitive to fast discharge pulses	Affected by multipath, shielding, metallic boundaries, and array placement
Acoustic	Less sensitive to electromagnetic interference	Requires a suitable propagation medium and stable structural coupling path
Optical or fiber-optic	Direct detection when the discharge is visible	Limited by line-of-sight, occlusion, and installation complexity
Conventional RSS or absolute amplitude/energy	Simple signal processing and ratio-based geometric formulation	Sensitive to source strength, channel gain, propagation model, and boundary coupling
Proposed electrostatic-induction feature-ratio method	Compact sensing heads, reduced TDOA dependence, and calibrated relative transient features	Requires geometry-specific calibration, environmental validation, and miniaturized electronics before deployment

6.6. Future Vacuum-Immersed System Development

Future work should extend the present proof-of-concept verification toward a vacuum-immersed and spacecraft-structure-representative system. The first step is to build a sealed or thermal-vacuum-compatible discharge test configuration in which the discharge source, sensing electrodes, cables, and front-end electronics can operate under controlled pressure and temperature. The second step is to introduce representative boundary structures, including metallic panels, dielectric samples, cable harnesses, grounding paths, and solar-array-interface analogs so that the calibration can include the dominant coupling paths expected in spacecraft compartments. The third step is to test the method under controlled plasma or charged-particle background conditions where sheath effects, surface-potential variation, and electrostatic screening can be assessed.

Several challenges are expected in this development. Vacuum operation may change the discharge inception process and pulse waveform, making it necessary to separate source-formation effects from localization errors. Plasma and charged-particle environments may change the baseline potential distribution and the effective coupling between the source and sensors. Thermal gradients may introduce gain drift, cable-impedance variation, dielectric-property changes, and mechanical deformation of the array geometry. Metallic cavities may shield or redirect the electric field, while dielectric surfaces may accumulate charge and introduce memory effects. These factors require an uncertainty budget that includes sensor-coordinate error, calibration residuals, feature noise, environmental drift, and boundary-coupling uncertainty. Future work should also optimize sensor number, placement, and array geometry and develop low-power integrated electronics for compact spacecraft monitoring.

7. Conclusions

This study developed a spacecraft-oriented electrostatic-induction sensor-array framework for three-dimensional localization of transient discharge events in confined spaces. A four-spherical-electrode array was used to acquire transient electric-field responses, and relative response representations were constructed to reduce sensitivity to source-strength variation and fixed channel differences. RMS, integrated energy, and envelope energy were compared as alternative feature scalings rather than as fully independent observables. Candidate-model screening indicated that the *Power + offset* mapping was a suitable compact feature-ratio–distance-ratio model for the calibrated domain. The calibrated mapping transformed multi-channel responses into Apollonius-sphere constraints, and nonlinear least-squares inversion provided the discharge coordinate estimate.

The method was evaluated on a 1 m^3 controlled confined-space laboratory platform with known sensor geometry. The envelope-energy representation achieved the best overall localization performance among the tested features, with a mean three-dimensional error of 7.01 cm, a median error of 6.94 cm, and a maximum error of 10.05 cm for ten independent test points. These results demonstrate the feasibility of the proposed sensing–calibration–inversion chain for reduced-timing-dependence discharge localization under the present laboratory conditions.

The limitations of this study are also clear. The present validation was conducted in ambient air with a needle–plate source and did not include vacuum, plasma, spacecraft materials, metallic enclosures, thermal gradients, or electronics integrated for spacecraft onboard operation. The 1 m^3 domain is a controlled validation volume rather than a direct physical model of a specific CubeSat or microsatellite. Because the method depends on empirical calibration, the reported localization accuracy should not be transferred directly to other spacecraft geometries or environments without recalibration. Future work will focus on vacuum-immersed testing, representative metallic and dielectric boundary structures, plasma and thermal effects, uncertainty-budget construction, optimized sensor placement, and miniaturized low-power electronics for spacecraft-oriented deployment validation.

Author Contributions: Conceptualization, K.T. and X.L.; methodology, K.T. and H.Z.; software, H.Z.; validation, K.T. and H.Z.; formal analysis, K.T. and H.Z.; investigation, K.T., H.Z. and X.S.; resources, X.S. and X.L.; data curation, H.Z.; writing—original draft preparation, K.T. and H.Z.; writing—review and editing, X.S. and X.L.; visualization, H.Z.; supervision, X.L.; project administration, X.L. All authors have read and agreed to the published version of the manuscript.

Funding: This research was funded by the Science and Technology on Reliability and Environmental Engineering Laboratory of China, grant number 2025-JCJQ-LB-047-04.

Institutional Review Board Statement: Not applicable.

Informed Consent Statement: Not applicable.

Data Availability Statement: The data presented in this study are available from the corresponding author upon reasonable request due to project-related restrictions.

Acknowledgments: The authors would like to express their sincere gratitude to all colleagues and technical staff who provided support in the experimental setup, measurement implementation, and data processing involved in this study. The authors also appreciate the valuable discussions and suggestions that helped improve the quality of this work.

Conflicts of Interest: The authors declare no conflicts of interest.

Abbreviations

The following abbreviations are used in this manuscript:

ESD	Electrostatic discharge
TDOA	Time difference of arrival
RMS	Root mean square
RSS	Received signal strength
RSSD	Received-signal-strength difference
AoA	Angle of arrival
MAE	Mean absolute error
SSE	Residual sum of squares
AICc	Corrected Akaike information criterion
UHF	Ultra-high frequency
HFCT	High-frequency current transformer
LM	Levenberg–Marquardt
EMC	Electromagnetic compatibility

References

1. Garrett, H.B. The charging of spacecraft surfaces. *Rev. Geophys. Space Phys.* **1981**, *19*, 577–616. [CrossRef]
2. Hastings, D.; Garrett, H. *Spacecraft-Environment Interactions*; Cambridge University Press: Cambridge, UK, 1996.
3. Lai, S.T. *Fundamentals of Spacecraft Charging: Spacecraft Interactions with Space Plasmas*; Princeton University Press: Princeton, NJ, USA, 2011.
4. National Aeronautics and Space Administration. *NASA-HDBK-4002B: Mitigating In-Space Charging Effects—A Guideline*; NASA: Washington, DC, USA, 2022.
5. European Cooperation for Space Standardization. *ECSS-E-ST-20-06C Rev.1: Spacecraft Charging*; ECSS Secretariat: Noordwijk, The Netherlands, 2019.
6. Wrenn, G.L. Conclusive evidence for internal dielectric charging anomalies on geosynchronous communications spacecraft. *J. Spacecr. Rocket.* **1995**, *32*, 514–520. [CrossRef] [PubMed]
7. Wrenn, G.L.; Rodgers, D.J.; Ryden, K.A. A solar cycle of spacecraft anomalies due to internal charging. *Ann. Geophys.* **2002**, *20*, 953–956. [CrossRef]
8. Minow, J.I.; Jordanova, V.K.; Pitchford, D.; Ganushkina, N.Y.; Zheng, Y.; Delzanno, G.L.; Jun, I.; Kim, W. ISWAT spacecraft surface charging review. *Adv. Space Res.* **2024**, *74*, 2863–2890. [CrossRef]
9. Horne, R.B.; Lam, P.Y.; Meredith, N.P.; Glauert, S.A.; Kirsch, P. Satellite internal charging for a reasonable worst-case. *Space Weather* **2025**, *23*, e2024SW004226. [CrossRef]
10. Purvis, C.K.; Garrett, H.B.; Whittlesey, A.C.; Stevens, N.J. *Design Guidelines for Assessing and Controlling Spacecraft Charging Effects*; NASA: Washington, DC, USA, 1984.
11. Garrett, H.B.; Whittlesey, A.C. *Guide to Mitigating Spacecraft Charging Effects*; Wiley: Hoboken, NJ, USA, 2012.
12. Yin, H.; Li, C.; Zhao, C.; Qin, X.; Lu, X.; Wen, X.; Shi, L.; Liu, Q.; Wang, J.; Jia, H.; et al. Research on monitoring methods for electrostatic discharge pulses in spacecraft dielectric materials. *Micromachines* **2025**, *16*, 180. [CrossRef] [PubMed]
13. Michelagnoli, M.; Focardi, M.; Pudney, M.; Renouf, I.; Merola, P.; Noce, V.; Nunez, M.V.; Dinuzzi, G.; Chiarucci, S. Surface charging analysis of Ariel spacecraft in L2-relevant space plasma environment and GEO early transfer orbit. *Aerospace* **2024**, *11*, 988. [CrossRef]
14. Yin, H.; Liu, H.; Qin, X.; Liu, Q.; Wang, J.; Wen, X.; Wang, P.; Yu, Z.; Yang, S. Research on high-precision and wide-range spacecraft potential measurement method based on capacitive voltage division. *Sensors* **2024**, *24*, 7583. [CrossRef] [PubMed]
15. Alvarez, F.; Garnacho, F.; Ortego, J.; Sánchez-Urán, M.Á. Application of HFCT and UHF sensors in on-line partial discharge measurements for insulation diagnosis of high-voltage equipment. *Sensors* **2015**, *15*, 7360–7387. [CrossRef] [PubMed]
16. Li, Z.; Luo, L.; Zhou, N.; Sheng, G.; Jiang, X. A novel partial discharge localization method in substation based on a wireless UHF sensor array. *Sensors* **2017**, *17*, 1909. [CrossRef] [PubMed]
17. Chan, J.Q.; Raymond, W.J.K.; Illias, H.A.; Othman, M. Partial discharge localization techniques: A review of recent progress. *Energies* **2023**, *16*, 2863. [CrossRef]
18. Patwari, N.; Ash, J.N.; Kyperountas, S.; Hero, A.; Moses, R.; Correal, N. Locating the nodes: Cooperative localization in wireless sensor networks. *IEEE Signal Process. Mag.* **2005**, *22*, 54–69. [CrossRef]
19. Tomic, S.; Beko, M.; Dinis, R. 3-D target localization in wireless sensor networks using RSS and AoA measurements. *IEEE Trans. Veh. Technol.* **2017**, *66*, 3197–3210. [CrossRef]

20. Lim, D.W.; Seo, J.H.; Chun, S.; Heo, M.B. A novel localization algorithm using received signal strength difference. *J. Position. Navig. Timing* **2017**, *6*, 141–147. [CrossRef]
21. Uluskan, S.; Filik, T. A geometrical closed form solution for RSS based far-field localization: Direction of exponent uncertainty. *Wirel. Netw.* **2019**, *25*, 215–227. [CrossRef]
22. Wang, Y.; Zhao, D.; Jia, Y.; Wang, S.; Du, Y.; Li, H.; Zhang, B. Acoustic sensors for monitoring and localizing partial discharges in oil-immersed transformers. *Sensors* **2024**, *24*, 4704. [CrossRef] [PubMed]
23. Liu, F.; Du, J.; Shi, Y.; Zhang, S.; Wang, W. Localization of dual partial discharge in transformer windings using Fabry–Perot optical fiber sensor array. *Energies* **2024**, *17*, 2537. [CrossRef]
24. Fan, X.; Qin, W.; Qiu, R.; Zang, Y.; Lu, W.; Zhang, Y.; Chen, R.; Liang, F.; Sun, G.; Luo, H.; et al. A review of advanced acoustic-chemical-optical partial discharge monitoring techniques for ultra-high-voltage gas-insulated equipment. *High Volt.* **2025**, *10*, 787–806. [CrossRef]
25. Tan, X.; Sun, H.; Suo, C.; Wang, K.; Zhang, W. Research of electrostatic field measurement sensors. *Ferroelectrics* **2019**, *549*, 172–183. [CrossRef]
26. Yan, Y.; Hu, Y.; Wang, L.; Qian, X.; Zhang, W.; Reda, K.; Wu, J.; Zheng, G. Electrostatic sensors—Their principles and applications. *Measurement* **2021**, *169*, 108506. [CrossRef]
27. Li, X.; Gu, Y.; Li, Z.; He, Z.; Yang, P.; Peng, C. A review of three-dimensional electric field sensors. *Micromachines* **2025**, *16*, 737. [CrossRef] [PubMed]
28. Jackson, J.D. *Classical Electrodynamics*, 3rd ed.; John Wiley & Sons: New York, NY, USA, 1999.
29. Griffiths, D.J. *Introduction to Electrodynamics*, 4th ed.; Cambridge University Press: Cambridge, UK, 2023.
30. Shockley, W. Currents to conductors induced by a moving point charge. *J. Appl. Phys.* **1938**, *9*, 635–636. [CrossRef]
31. Smythe, W.R. *Static and Dynamic Electricity*, 3rd ed.; Hemisphere Publishing: New York, NY, USA, 1989.
32. The CubeSat Program, California Polytechnic State University. *CubeSat Design Specification Rev.14*; California Polytechnic State University: San Luis Obispo, CA, USA, 2022.
33. European Space Agency. Proba-1 Overview. Available online: https://www.esa.int/Applications/Observing_the_Earth/Proba-1_overview (accessed on 23 May 2026).
34. European Space Agency. Proba-2: Spacecraft. Available online: https://www.esa.int/Enabling_Support/Space_Engineering_Technology/Proba_Missions/Proba-2_Spacecraft (accessed on 23 May 2026).
35. European Cooperation for Space Standardization. *ECSS-E-ST-20C Rev.2: Space Engineering—Electrical and Electronic*; ECSS Secretariat: Noordwijk, The Netherlands, 2022.
36. European Cooperation for Space Standardization. *ECSS-E-ST-20-07C Rev.2: Space Engineering—Electromagnetic Compatibility*; ECSS Secretariat: Noordwijk, The Netherlands, 2022.

Disclaimer/Publisher's Note: The statements, opinions and data contained in all publications are solely those of the individual author(s) and contributor(s) and not of MDPI and/or the editor(s). MDPI and/or the editor(s) disclaim responsibility for any injury to people or property resulting from any ideas, methods, instructions or products referred to in the content.